

# Bidirectional Cross-Perception for Open-Vocabulary Semantic Segmentation in Remote Sensing Imagery

Jianzheng Wang<sup>1</sup> Huan Ni<sup>\*1</sup>

## Abstract

High-resolution remote sensing imagery is characterized by densely distributed land-cover objects and complex boundaries, which places higher demands on both geometric localization and semantic prediction. Existing training-free open-vocabulary semantic segmentation (OVSS) methods typically fuse CLIP and vision foundation models (VFs) using “one-way injection” and “shallow post-processing” strategies, making it difficult to satisfy these requirements. To address this issue, we propose a spatial-regularization-aware dual-branch collaborative inference framework for training-free OVSS, termed SDCI. First, during feature encoding, SDCI introduces a cross-model attention fusion (CAF) module, which guides collaborative inference by injecting self-attention maps into each other. Second, we propose a bidirectional cross-graph diffusion refinement (BCDR) module that enhances the reliability of dual-branch segmentation scores through iterative random-walk diffusion. Finally, we incorporate low-level superpixel structures and develop a convex-optimization-based superpixel collaborative prediction (CSCP) mechanism to further refine object boundaries. Experiments on multiple remote sensing semantic segmentation benchmarks demonstrate that our method achieves better performance than existing approaches. Moreover, ablation studies further confirm that traditional object-based remote sensing image analysis methods leveraging superpixel structures remain effective within deep learning frameworks. Code: <https://github.com/yu-ni1989/SDCI>.

<sup>\*</sup>Equal contribution <sup>1</sup> School of Remote Sensing & Geomatics Engineering, Nanjing University of Information Science & Technology, Nanjing, China. Correspondence to: Huan Ni <nih@nuist.edu.cn>.

Preprint Version. Copyright 2026 by the author(s).

## 1. Introduction

Vision-language models (VLMs) and vision foundation models (VFs) have been leveraged to meet the objective of open-vocabulary semantic segmentation (OVSS) (Ge et al., 2025). Existing approaches can be classified as training-based (Zhong et al., 2025) and training-free (Shi et al., 2025; Zhang et al., 2025b) methods. Compared with training-based approaches, training-free methods are more flexible, and require no expensive manual annotations, thus showing great application potential. However, extending training-free OVSS techniques to the remote sensing domain poses unique challenges. Compared with natural images, high-resolution remote sensing imagery typically exhibits a top-down “bird’s-eye view” perspective, characterized by densely distributed ground objects, drastic scale variations, and extremely complex boundaries. Such differences imply that remote sensing tasks impose stricter requirements on both geometric localization and semantic descriptions.

On the one hand, as a representative VLM, the Contrastive Language-Image Pretraining (CLIP) (Radford et al., 2021) which can generate high-level semantics in a zero-shot setting by leveraging text prompts, is widely used. To meet the objective of OVSS, existing works mainly focus on modifying CLIP’s internal attention mechanism, such as ClearCLIP (Lan et al., 2025) and CLIPer (Sun et al., 2025). However, CLIP is mainly designed for image-level classification, and thus lacks pixel-level spatial localization ability, leading to the difficulty for precise geometric positional information (such as pixel-level boundaries) acquisition in remote sensing tasks. On the other hand, VFs such as DINO (Caron et al., 2021) and SAM (Kirillov et al., 2023) have been widely adopted in foreground object segmentation tasks (Siméoni et al., 2021; 2022; Wang et al., 2022). Although VFs excel at modeling spatial details, their learned embedding spaces are not explicitly aligned with textual semantics, and thus they lack semantic description capability tailored to remote sensing tasks. To capitalize on the strengths of CLIP and VFs while mitigating their shortcomings, some studies have begun to explore integrating them. For example, ProxyCLIP (Lan et al., 2024) borrows attention maps from external VFs to guide CLIP, and CorrCLIP (Zhang et al., 2025a) leverages VFs to estimate the

interaction range of similarity-based patch relations, thereby reducing inter-class correlation. We summarize this line of work as a “one-way injection” from VFM to CLIP, or from CLIP to VFM. In addition, some approaches conduct fusion in the output space using masking (Barsellotti et al., 2024b), graph matching (Kim et al., 2025), or the strategy that employing independently pretrained modules (Li et al., 2025). These methods typically treat VFM or vision operators as a static “black box”, using only their outputs for fusion and post-processing. We summarize this line of work as “shallow post-processing”. The “one-way injection” and “shallow post-processing” fail to achieve deep, bidirectional fusion, leading to inferior results in segmenting remote sensing images.

Meanwhile, we observe that superpixel structures naturally enhance object boundaries, which can effectively compensate for CLIP’s limitations in pixel-level spatial localization ability in remote sensing tasks. As illustrated in Fig. 1(a)–(b), the superpixels closely adhere to the physical contours of objects; in contrast, the segmentation produced by CLIPer (Sun et al., 2025) in Fig. 1(c) remains blurry near boundaries and fails to precisely distinguish different land-cover categories. This comparison indicates that the low-level geometric priors carried by superpixels are crucial for addressing the “blurry-boundary” issue.

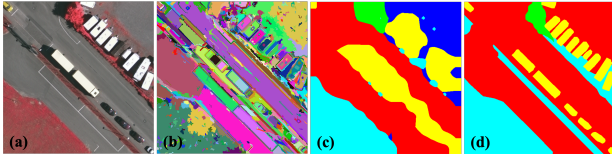


Figure 1. Observation on the boundary-enhancing effect of superpixels. (a) original remote sensing image, (b) superpixel segmentation result; (c) semantic segmentation result generated by CLIPer, (d) ground truth.

On top of these observations, we propose a novel spatial-regularization-aware dual-branch collaborative inference framework for OVSS in a training-free manner, termed SDCI. SDCI consists of three core collaborative components, i.e., a cross-model attention fusion (CAF) module and a bidirectional cross-graph diffusion-based refinement (BCDR) module, together with a convex-optimization-based superpixel collaborative prediction (CSCP) mechanism. Specifically, CAF performs bidirectional injection of attention maps during feature encoding, enabling CLIP’s semantic predictions to be propagated with DINO’s structural information, while simultaneously enriching DINO’s structural perception with CLIP’s semantic cues. Based on this interaction, we obtain high-quality initial segmentation results. Then, BCDR places the initial results into a global refinement process via iterative random-walk diffusion: it

uses the “structural graph” constructed by DINO to correct spatial inconsistencies in CLIP, and uses the “semantic graph” constructed by CLIP to merge semantically separated regions in DINO. Finally, considering the complex boundaries of ground objects and the high geometric-precision requirement in remote sensing imagery, we introduce superpixel structures and convex optimization to deeply fuse the initial segmentation outputs from both the CLIP and DINO branches. Extensive experiments demonstrate the effectiveness of our method, and our contributions are summarized as follows:

- CAF and BCDR that enable bidirectional interaction between CLIP’s semantic knowledge and DINO’s structural information are proposed. The two modules address both the “one-way injection” and “shallow post-processing” issues, exchanging complementary information and mitigating noise interference.
- CSCP that formulates a global energy minimization framework and introduces superpixels as a strong geometric constraint is proposed. CSCP deeply integrates the semantic probability predictions produced by CLIP and DINO with low-level superpixel topology to precisely sharpen segmentation boundaries, which further addresses the “shallow post-processing” issue.
- Building on the above modules, we present a novel training-free collaborative inference framework, SDCI. By deeply fusing information at both the feature encoding stage and the segmentation refinement stage, the proposed framework hierarchically improves OVSS performance, achieving superior results over existing methods on multiple remote sensing semantic segmentation benchmarks.

## 2. Related Work

### 2.1. Methods based on improving internal mechanisms of CLIP.

The central idea of this line of research is to exploit and rectify the attention mechanisms within CLIP itself, making it suitable for pixel-level tasks (Hajimiri et al., 2025; Shao et al., 2025; Sun et al., 2023). For example, MaskCLIP (Zhou et al., 2022) employs an identical self-self matrix as the self-attention map at last layer to generate visual patch embeddings. SCLIP (Wang et al., 2025) and ClearCLIP (Lan et al., 2025) introduce self-self attention variants to replace the original query-key attention, thereby improving the spatial consistency of feature maps. Different from those approaches that completely discard query-key interactions, ResCLIP (Yang et al., 2025) extracts cross-correlation features preserved in intermediate layers and restores the spatial localization capability of the last layer

via residual connections. However, as pointed out by the fine-grained analysis in clip-oscope (Abbasi et al., 2025), CLIP exhibits significant biases toward large objects and specific text ordering in multi-object scenes. Such inherent deficiencies in spatial and structural perception make it difficult for purely internal correction methods in CLIP to achieve accurate boundary localization in remote sensing scenarios.

## 2.2. Methods using only VFMs.

Leveraging the robust visual representations of DINO series (Caron et al., 2021; Oquab et al., 2024; Siméoni et al., 2025), researchers have developed several unsupervised segmentation methods. TokenCut (Wang et al., 2023b) constructs a fully connected graph based on image features and segments salient objects using the Normalized Cut algorithm (Shi & Malik, 2000). CutLER (Wang et al., 2023a; 2024) extends this idea by discovering multiple objects from self-supervised features, enabling zero-shot unsupervised localization. Meanwhile, SAM series (Kirillov et al., 2023; Ravi et al., 2024) demonstrates remarkable category-agnostic segmentation capability. Subsequently, improved SAM-based methods, such as E-SAM (Zhang et al., 2025b) and OmniSAM (Zhong et al., 2025), have enhanced segmentation completeness and accuracy to varying degrees. However, the “structure without semantics” property prevents them from independently solving OVSS, highlighting the necessity of collaborating with CLIP.

## 2.3. Multi-model collaborative methods.

Firstly, some approaches attempt to support segmentation by constructing external data assistance, such as ReCo (Shin et al., 2022), OVDiff (Karazija et al., 2025), FOSSIL (Barsellotti et al., 2024a), and FreeDA (Barsellotti et al., 2024b). However, these methods need large-scale retrieval and offline generation (Rombach et al., 2022), which introduces substantial computational overhead and pipeline complexity. Other approaches focus on aligning features across models by employing learnable parameters (Barsellotti et al., 2025; Wysoczańska et al., 2025). Although effective, introducing learnable parameters sacrifices the pure training-free flexibility.

In contrast, some works explore fully training-free strategies using both CLIP and VFMs (Kang & Cho, 2024; Lan et al., 2024; Zhang et al., 2025a). Specifically, CASS (Kim et al., 2025) further proposes injecting features from DINO into the attention mechanism of CLIP to enhance object-level contextual consistency. SegEarth-OV (Li et al., 2025) improves FeatUp (Fu et al., 2024) and introduces the independently pretrained SimFeatUp for post-processing. However, these methods often rely on “one-way information injection” or “shallow post-processing”, and fail to achieve deep

fusion between the two models.

## 3. Methodology

### 3.1. Overview

Figure 2 illustrates the overall architecture of SDCI. SDCI mainly consists of three core components: CAF, BCDR and CSCP. The detailed description of these modules is shown in Appendix A.

### 3.2. CAF

CAF first processes the input image in parallel using the CLIP image encoder and DINO, and then performs cross-fusion on top of them.

**Semantic Branch.** To enhance the spatial consistency of patch embeddings, we adopt a multi-level feature fusion strategy similar to CLIPer (Sun et al., 2025). Given the patch embedding  $F_{0,clip} \in \mathbb{R}^{(hw+1) \times D}$ , we feed it into a stack of Transformer blocks. For the  $n$ -th Transformer block, the output embedding  $F_{n,clip}$  is computed via standard self-attention  $\text{Att}(\cdot)$  and feed-forward networks  $\text{FFN}(\cdot)$ :

$$F'_{n,clip} = \text{Att}(Q_n, K_n, V_n) + F_{n-1,clip}, \quad (1)$$

$$F_{n,clip} = \text{FFN}(\text{LN}(F'_{n,clip})) + F'_{n,clip}, \quad (2)$$

where  $Q_n$ ,  $K_n$ , and  $V_n$  denote the query, key, and value matrices obtained by linearly projecting  $F_{n-1,clip}$ .  $\text{LN}(\cdot)$  is a normalization layer. The attention map at each layer is computed as

$$A_n = \text{Softmax}\left(\frac{Q_n K_n^\top}{\sqrt{d_k}}\right), \quad (3)$$

where  $d_k$  is the feature dimension of each attention head. To leverage the rich spatial information from early layers, we collect and average the attention maps of all intermediate layers to obtain an averaged attention map:

$$A_{\text{avg}} = \frac{1}{N-1} \sum_{n=1}^{N-1} A_n. \quad (4)$$

We then use  $A_{\text{avg}}$  as a spatial prior to guide the feature processing in the  $N$ -th layer:

$$F_{N,clip} = \text{Norm}\left(\text{ReLU}(\text{Sym}(A_{\text{avg}}) - \mu)\right) \cdot V_N, \quad (5)$$

where  $\text{Sym}(\cdot)$  denotes the symmetrization operation, and  $\mu$  is the mean value of  $A_{\text{avg}}$ .  $\text{Norm}(\cdot)$  denotes  $\ell_1$  normalization, and  $\text{ReLU}(\cdot)$  sets negative values to zero. This process yields the final feature embeddings  $\{F_{1,clip}, \dots, F_{N,clip}\}$  for the semantic branch. Moreover, we average  $A_{\text{avg}}$  across

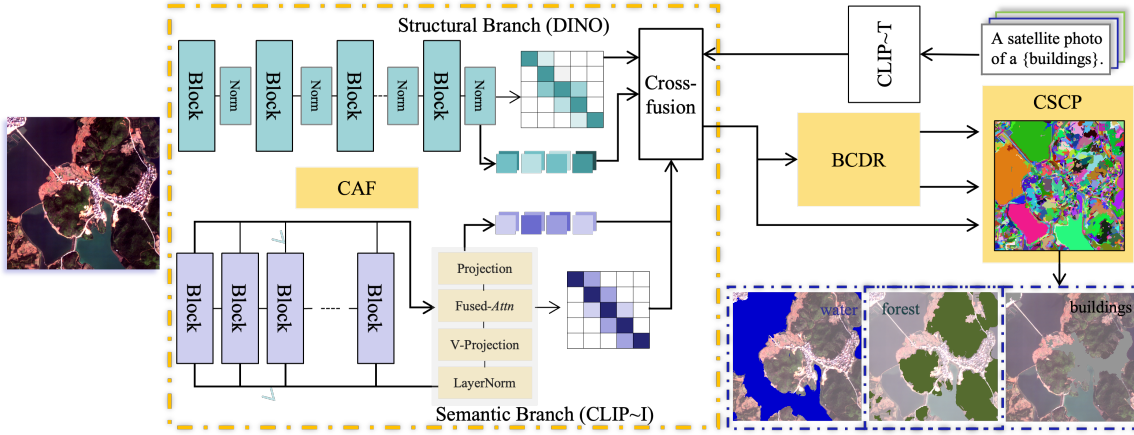


Figure 2. The proposed SDCI framework, in which CAF, BCDR, and CSCP serve as the core modules. CAF enables interaction between semantic and structural information by exchanging attention maps. The resulting initial logit maps are then fed into the BCDR module, which performs cross diffusion between the structural graph constructed by DINO and the semantic graph constructed by CLIP to achieve globally consistent enhancement. Finally, CSCP imposes constraints from superpixel structures and, through a convex optimization process, fuses the predictions from the two branches to generate the final segmentation map.

the head dimension to obtain the effective attention map  $A_{N,clip}$ :

$$A_{N,clip} = \frac{1}{H} \sum_{h=1}^H A_{avg}^{(h)}, \quad (6)$$

where  $H$  is the number of heads in multi-head attention, and  $A_{avg}^{(h)}$  denotes the component of  $A_{avg}$  in the  $h$ -th head.

**Structural Branch.** In parallel, we process the same input image using the DINO visual encoder. Different from the fusion strategy adopted in the semantic branch, our strategy for the structural branch is to maximally preserve its original high-quality hierarchical structural information. For the output feature  $F'_{n,dino}$  from the  $n$ -th Transformer block, before collecting it, we pass it through a normalization layer to obtain the normalized feature  $F_{n,dino}$ , which can be formulated as

$$F_{n,dino} = \text{Norm}(F'_{n,dino}), \quad \forall n \in \{1, \dots, N\}. \quad (7)$$

This ensures that features from low to high layers are mapped into a normalized and stable feature space. We then stack these normalized hierarchical features to form a full-level feature tensor  $\{F_{1,dino}, \dots, F_{N,dino}\}$ . Meanwhile, we extract the standard self-attention map from the last Transformer block, denoted as  $A_{N,dino}$ .

**Cross-Fusion.** After extracting the hierarchical features and attention maps from both branches via the above asymmetric strategies, knowledges are fused. First, we spatially align the final effective attention maps of the two branches. Meanwhile, we compare the full-level

features  $\{F_{1,clip}, \dots, F_{N,clip}\}$  and  $\{F_{1,dino}, \dots, F_{N,dino}\}$  with the text embedding  $E_T$ , obtaining the corresponding full-level segmentation logits  $\{S_{1,clip}, \dots, S_{N,clip}\}$  and  $\{S_{1,dino}, \dots, S_{N,dino}\}$ . Notably, although the feature space of DINO is not explicitly aligned with text, the intrinsic structure emerging from its high-quality visual representations enables the comparison with  $E_T$  to still produce meaningful initial segmentation results rich in spatial details.

Next, we compute the final preliminary segmentation scores using a cross-fusion formulation. For the semantic branch, the enhanced score  $S'_{clip}$  is computed as

$$S'_{clip} = \left( \text{Align}(A_{N,clip}) + \lambda_1 \cdot \text{Align}(A_{N,dino}) \right) \cdot S_{N,clip} + \frac{1}{N-1} \sum_{n=1}^{N-1} S_{n,clip}. \quad (8)$$

Here,  $\text{Align}(\cdot)$  denotes a spatial alignment operator, and  $\lambda_1$  is a hyperparameter used to balance the strength of structured guidance from DINO (we set  $\lambda_1 = 1$  by default). The terms  $S_{N,clip}$ ,  $S_{n,clip}$  and  $A_{N,clip}$  are obtained from the semantic branch described above.

Similarly, the cross-fusion for the structural branch follows the similar way, and the produced score  $S'_{dino}$  is computed as

$$S'_{dino} = \left( \text{Align}(A_{N,dino}) + \lambda_1 \cdot \text{Align}(A_{N,clip}) \right) \cdot S_{N,dino} + \frac{1}{N-1} \sum_{n=1}^{N-1} S_{n,dino}. \quad (9)$$

The inputs  $S_{N,\text{dino}}$ ,  $S_{n,\text{dino}}$  and  $A_{N,\text{dino}}$  are obtained from the structural branch, while all other symbols and parameters share the same definitions as those in Eq. 8. The enhanced effect after bidirectional injection of the attention maps in the Eq. 8 and Eq. 9 is shown in Appendix B. In summary, through CAF that combines high-level guidance with full-level aggregation, our method achieves a favorable balance between the accuracy of semantic decision-making and the fidelity of spatial details, producing high-quality initial segmentation results for the subsequent BCDR.

### 3.3. BCDR

To achieve global enhancement of the preliminary segmentation logits, BCDR first explicitly models the discrete image patches in the spatial domain as a graph structure. Furthermore, since different models perceive different intrinsic relationships within an image, we can construct a semantic graph and a structural graph, which respectively serve different objectives for the enhancement.

**Semantic Graph Construction.** The semantic graph is constructed from the semantic branch. Given the CLIP features  $\{F_{1,\text{clip}}, \dots, F_{N,\text{clip}}\}$ , we compute

$$F_{\text{clip}} = \frac{1}{N} \sum_{i=1}^N F_{i,\text{clip}}. \quad (10)$$

After applying  $\ell_2$  normalization, each vector in  $F_{\text{clip}}$  has unit norm, which ensures that  $F_{\text{clip}} F_{\text{clip}}^\top$  becomes a pairwise cosine-similarity matrix. Accordingly, the transition matrix  $T_{\text{clip}}$  is defined as

$$T_{\text{clip}} = \text{Norm}_{\text{row}} \left( \exp \left( \frac{S_K(F_{\text{clip}} F_{\text{clip}}^\top)}{\tau} \right) \right). \quad (11)$$

Here, the cosine similarities in  $F_{\text{clip}} F_{\text{clip}}^\top$  define the affinities between nodes. The operator  $S_K(\cdot)$  denotes a  $K$ -nearest-neighbor sparsification, which retains only the top- $K$  non-diagonal similarities in each row and sets all remaining entries to  $-\infty$ . The parameter  $\tau$  is a temperature scaling coefficient that controls the sharpness of affinity weights, and is set to 0.07 by default in this work. The function  $\exp(\cdot)$  converts the sparsified similarities into non-negative affinity weights. Finally,  $\text{Norm}_{\text{row}}(\cdot)$  denotes row-wise normalization, ensuring that each row sums to 1.

**Structural Graph Construction.** Based on the DINO features  $\{F_{1,\text{dino}}, \dots, F_{N,\text{dino}}\}$ , we define the structural graph transition matrix  $T_{\text{dino}}$ , whose edge weights strongly reflect pixel-level physical connectivity, as

$$T_{\text{dino}} = \text{Norm}_{\text{row}} \left( \exp \left( \frac{S_K(F_{\text{dino}} F_{\text{dino}}^\top)}{\tau} \right) \right). \quad (12)$$

The definitions of all symbols follow the same procedure as in the computation of  $T_{\text{clip}}$ .

**Bidirectional refinement.** Given  $T_{\text{clip}}$  and  $T_{\text{dino}}$ , BCDR designs a novel cross-graph diffusion mechanism to perform global refinement with complementary strengths. This mechanism smooths the preliminary segmentation logits via an iterative random-walk process. Specifically, the refinement is bidirectional and symmetric: we use  $T_{\text{dino}}$  to refine the CLIP semantic scores  $S'_{\text{clip}}$ , and use  $T_{\text{clip}}$  to refine the DINO structural scores  $S'_{\text{dino}}$ .

For the semantic branch, the scores after  $t$  diffusion steps, denoted as  $S_{\text{clip}}^{(t)}$ , are computed as

$$S_{\text{clip}}^{(t)} = \alpha T_{\text{dino}} S_{\text{clip}}^{(t-1)} + (1 - \alpha) S'_{\text{clip}}. \quad (13)$$

Symmetrically, for the structural branch, the scores after  $t$  diffusion steps, denoted as  $S_{\text{dino}}^{(t)}$ , are computed as

$$S_{\text{dino}}^{(t)} = \alpha T_{\text{clip}} S_{\text{dino}}^{(t-1)} + (1 - \alpha) S'_{\text{dino}}. \quad (14)$$

Here,  $\alpha \in (0, 1)$  is a smoothing factor that balances neighborhood propagation and the initial information, and we set  $\alpha = 0.9$  by default in this work. We set the total diffusion steps  $T$  to 40, and the final enhanced scores are defined as

$$S_{g\text{-clip}} = S_{\text{clip}}^{(T)}, \quad S_{g\text{-dino}} = S_{\text{dino}}^{(T)}. \quad (15)$$

In this way, we enforce the CLIP semantic predictions to propagate along the accurate physical paths depicted by DINO, thereby enhancing spatial consistency. Meanwhile, we leverage the CLIP semantic graph to merge regions in the DINO predictions that may be separated due to appearance variations, ensuring semantic completeness. Equations (13)–(15) finally output two enhanced scores, namely  $S_{g\text{-clip}}$  and  $S_{g\text{-dino}}$ , providing higher-quality inputs for the final CSCP stage.

### 3.4. CSCP

To enforce the final segmentation map to be locally consistent with the low-level natural structures of the image, while also fusing the predictions from the two parallel branches, we propose a convex optimization-based superpixel collaborative prediction mechanism, namely CSCP.

First, we adopt the Felzenszwalb algorithm (Felzenszwalb & Huttenlocher, 2004) to decompose the input image  $I$  into a set of superpixels  $S = \{s_1, \dots, s_M\}$ . Then, using the topology of these superpixels, we construct a graph structure  $W$  with adaptive edge weights. Specifically, for any adjacent pixel pair  $(p, q)$  in the image, the connection weight  $w_{p,q}$  is defined as

$$w_{p,q} = w_{\text{cross}} + (w_{\text{in}} - w_{\text{cross}}) \cdot \mathbb{I}(s(p) = s(q)), \quad (16)$$

where  $s(\cdot)$  denotes the superpixel index mapping such that, for a pixel  $p$ , if  $p \in s_i$  (i.e., pixel  $p$  belongs to the  $i$ -th superpixel in  $S$ ), then  $s(p) = i$ . The function  $\mathbb{I}(\cdot)$  is an indicator function that equals 1 when the condition holds and 0 otherwise. In our experiments, we set  $w_{\text{in}} = 1.0$  and  $w_{\text{cross}} = 0.10$ . Within each superpixel, pixels are assigned larger connection weights to impose smoothness constraints; across superpixel boundaries, the weights are significantly reduced, allowing gradient discontinuities in the segmentation map and thus preserving object contours.

Next, we take the globally refined predictions from BCDR, namely the CLIP output  $S_{g\text{-clip}}$  and the DINO output  $S_{g\text{-dino}}$ , as inputs. We construct a global energy function  $E(Q)$ , aiming to find an optimal probability distribution  $Q$  that satisfies both semantic consistency and geometric smoothness. The optimization problem is formulated as

$$\begin{aligned} \min_{Q \in \Delta} E(Q) = & \sum_{p \in \Omega} [\lambda_C \text{KL}(Q_p \| S_{g\text{-clip}}(p)) + \\ & \lambda_D \text{KL}(Q_p \| S_{g\text{-dino}}(p)) + \\ & \beta \sum_{(p,q) \in \varepsilon} w_{p,q} \|Q_p - Q_q\|_1], \end{aligned} \quad (17)$$

where  $Q$  is the target refined probability distribution to be optimized, and  $Q_p \in \mathbb{R}^K$  denotes the  $K$ -dimensional class probability vector at pixel  $p$ . The set  $\Omega$  represents the image domain (i.e., the set of all pixels). The symbol  $\Delta$  denotes the simplex constraint, defined as

$$\Delta = \left\{ Q \left| \sum_{k=1}^K Q_p^k = 1, Q_p^k \geq 0 \right. \right\}, \quad (18)$$

which guarantees that the optimized result satisfies the mathematical properties of a valid probability distribution. The divergence  $\text{KL}(\cdot \| \cdot)$  denotes the Kullback–Leibler divergence, which measures the information discrepancy between the refined distribution  $Q$  and the original predictions. The coefficients  $\lambda_C$  and  $\lambda_D$  are balancing factors that adjust the confidence assigned to the two branch predictions; in our experiments, we set  $\lambda_C = 1.0$  and  $\lambda_D = 0.2$ . The parameter  $\beta$  is a regularization weight that controls the overall strength of spatial smoothness. The set  $\varepsilon$  contains all adjacent pixel pairs on the image grid. The adaptive weight  $w_{p,q}$  is generated from the superpixel prior using Eq. 16. The norm  $\|\cdot\|_1$  denotes the  $\ell_1$  norm. Due to that the above energy function  $E(Q)$  contains a non-smooth total variation term, we adopt the Primal–Dual Hybrid Gradient (PDHG) algorithm (Chambolle & Pock, 2011) to solve it iteratively, which guarantees convergence to the global optimum.

## 4. Experiment

The details of experimental settings are shown in Appendix C.

### 4.1. Prompt Settings

To conduct a more rigorous and realistic evaluation of model performance, we design two prompt settings: *original-label* and *generalized-label* settings. The details of the design process are presented in Appendix C.4.

**Original-Label (Ori) Setting:** We directly use the category names officially provided by each dataset as text prompts. This setting is mainly adopted to measure the benchmark performance under professional land-cover terminology.

**Generalized-Label (Gen) Setting:** This setting aims to systematically bridge the semantic gap between the official category names and the vocabulary space of CLIP. Official category names are often sub-optimal text prompts because they can be overly specialized (e.g., *impervious surfaces*) or conceptually abstract (e.g., *agriculture*), making them difficult to align with CLIP’s natural-language-based understanding paradigm.

### 4.2. Comparison with Other Methods

As shown in Table 1, under the original-label setting, SDCI-v2 demonstrates outstanding overall performance, achieving an average mIoU of 48.49% and outperforming all competing methods. For instance, on the GID dataset, SDCI-v2 (Ori) attains an mIoU of 59.59%, surpassing the previous state-of-the-art method CASS (57.73%). On the Vaihingen dataset, SDCI-v2 (33.69%) significantly exceeds the second-best method CLIPer (26.21%). Under the generalized-label setting, SDCI consistently maintains its advantage. For example, on the Potsdam dataset, the score of SDCI-v2 surges from 36.47% in the Ori setting to 57.51% in the Gen setting, which not only substantially surpasses its own benchmark performance but also exceeds ResCLIP (53.31%) under the same setting by 4.20%. This result indicates that our framework is able to flexibly handle different forms of text prompts.

In addition to its superior segmentation accuracy, our model is also acceptable in computational efficiency. Under a unified input resolution of  $512 \times 512$ , we evaluate the computational complexity of different SDCI variants and existing methods. Specifically, SDCI-v1 adopts the  $8 \times 8$  patch strategy of DINO-v1, which significantly increases the feature sequence length and thus incurs a higher computational cost (1995.87 GFLOPs). In contrast, the best-performing SDCI-v2 (with a  $14 \times 14$  patch strategy) successfully reduces the computation to 1656.44 GFLOPs while preserving sufficient spatial details. This cost is only about 1/16 of that of the highly compute-intensive model CASS (26943.79 GFLOPs), and it also avoids the severe performance degradation observed in the lightweight model NA-CLIP (242.96 GFLOPs), which achieves only 20.93% mIoU on Vaihingen. Although SDCI-v2 requires slightly more

Table 1. Quantitative comparison with existing methods on GID, Potsdam, Vaihingen, LoveDA, and iSAID. Values are mean Intersection-over-Union (mIoU, %). Ori and Gen denote the prompt settings with Original Labels and Generalized Labels, respectively. GFLOPs are measured under a fixed input resolution of  $512 \times 512$ . SDCI-v1 and SDCI-v2 correspond to integrating DINO-v1 (ViT-B/8) and DINO-v2 (ViT-B/14) as the structural branch, respectively. Best results are in **bold**; second-best results among existing methods are underlined. Blue numbers indicate the absolute improvement over the second-best method.

Method	GID		Potsdam		Vaihingen		LoveDA		iSAID	Avg	GFLOPs
	Ori	Gen	Ori	Gen	Ori	Gen	Ori	Gen	Ori		
MaskCLIP (Zhou et al., 2022)	45.04	52.06	26.54	46.76	24.80	35.15	38.37	36.90	14.50	35.57	2944.88
ClearCLIP (Lan et al., 2025)	53.03	58.71	26.29	46.88	22.01	26.69	38.39	39.51	18.20	36.63	2953.55
SCLIP (Wang et al., 2025)	52.80	58.50	27.13	49.93	22.72	30.23	37.05	37.85	16.10	36.92	2926.29
CorrCLIP (Zhang et al., 2025a)	50.00	45.73	25.53	43.28	23.00	43.42	34.08	33.62	25.50	36.02	6424.47
CLIPer (Sun et al., 2025)	52.11	<u>66.85</u>	25.96	45.22	<u>26.21</u>	<u>43.97</u>	<u>43.58</u>	<u>43.84</u>	27.36	41.68	4615.63
NACLIP (Hajimiri et al., 2025)	54.96	63.29	<u>33.47</u>	32.03	20.93	<u>33.14</u>	32.29	32.20	31.57	37.10	242.96
ResCLIP (Yang et al., 2025)	54.23	60.67	27.02	<u>53.31</u>	23.39	38.32	39.88	40.85	<u>43.79</u>	<u>42.38</u>	1029.66
CASS (Kim et al., 2025)	<u>57.73</u>	57.73	32.68	34.28	24.21	41.14	42.42	42.01	40.41	40.41	26943.79
SegEarth-OV (Li et al., 2025)	52.49	59.49	30.63	48.80	23.03	39.34	40.97	42.63	21.70	39.90	1124.28
SDCI-v1 (Ours)	58.93	<b>71.15</b>	32.37	57.74	33.21	45.24	<b>44.89</b>	<b>45.19</b>	45.67	48.27	2022.72
	(+1.20)	(+4.30)	(—)	(+4.43)	(+7.00)	(+1.27)	(+1.31)	(+1.35)	(+1.88)	(+5.89)	
SDCI-v2 (Ours)	<b>59.59</b>	66.40	<b>36.47</b>	<b>57.51</b>	<b>33.69</b>	<b>50.08</b>	43.70	42.62	<b>46.37</b>	<b>48.49</b>	1683.29
	(+1.86)	(—)	(+3.00)	(+4.20)	(+7.48)	(+6.11)	(+0.12)	(—)	(+2.58)	(+6.44)	

computation than SegEarth-OV (1124.28 GFLOPs), this increase is justified given the substantial performance gains it delivers.

A particularly notable finding is that the significant improvement brought by generalized labels (Gen) stems from the fact that their textual descriptions closely match the pretraining distribution preferences and the demand for semantic concreteness of VLMs. Since models such as CLIP are trained on massive amounts of natural language from the Internet, their feature space is more sensitive to and better aligned with common, high-frequency, and concrete words, while responding more weakly to low-frequency, abstract, and specialized terms. Generalized labels effectively transform complex expert-level geoscience categories into intuitive visual-attribute descriptions, substantially reducing semantic ambiguity and enabling the high-level semantic features extracted by CLIP to be activated and retrieved more precisely. The visual comparison is shown in Appendix D.

### 4.3. Ablation Study

To ensure fair and meaningful comparisons, we adopt a strong CLIP-based baseline built upon multi-level feature fusion. This baseline follows the core ideas of CLIPer (Sun et al., 2025) and clearCLIP (Lan et al., 2025), aiming to alleviate the limited spatial localization capability of standard CLIP by exploiting early-layer features. In addition, it simplifies the network structure of the final layer to reduce noise and better align visual features with text embeddings, thereby establishing a strong baseline that outper-

Table 2. Ablation results of different modules in SDCI on the GID dataset. The metric is mIoU (%). The meaning of “Set of Gen” is introduced in detail in Appendix C.4

Method	Ori	Gen	Set of Gen
Baseline	49.75	56.82	57.58
Baseline + DINO-v1 (Late Fusion)	45.76	55.60	53.68
Baseline + CAF	53.40	61.86	58.22
	(+3.65)	(+5.04)	(+0.64)
Row 3 + BCDR	58.09	62.46	58.65
	(+8.34)	(+5.64)	(+1.07)
Row 4 + CSCP (Ours, DINO-v1)	58.93	71.15	64.17
	(+9.18)	(+14.33)	(+6.59)
Row 4 + CSCP (Ours, DINO-v2)	<b>59.59</b>	66.40	64.10
	(+9.84)	(+9.58)	(+6.52)

forms vanilla CLIP. Starting from this baseline, we conduct a progressive and incremental ablation study to quantify the contribution of each core component in SDCI. The results are reported in Table 2.

**Effectiveness of Core Components.** Under the original-label setting, our method exhibits a clear performance ladder. Starting from the baseline (49.75%), the mIoU steadily increases to 59.59% after progressively adding the CAF, BCDR, and CSCP modules. This consistent upward trend strongly demonstrates that each module is effective and makes a significant contribution. In the Gen and Set of Gen settings, when CSCP is integrated, the accuracy improves substantially, rising from 62.46% (58.65%) to

71.15% (64.17%). This highlights the significant contribution of CSCP and demonstrates that the geometric constraints induced by the superpixel structure are highly effective. This naturally brings to mind the once-popular but now largely overlooked object-based remote sensing image analysis strategy built on superpixels. The success of CSCP suggests that traditional object-based remote sensing processing paradigms can still play a positive role within deep learning frameworks. The visual results of the ablation study is shown in Appendix E.

**Necessity of Simple Late Fusion Strategy.** An insightful phenomenon appears in the second row in Table 2. When adopting a simple late fusion strategy—i.e., directly summing the semantic scores of DINO and CLIP with fixed weights—the performance under the Ori setting drops from 49.75% to 45.76%. We attribute this to the fact that although DINO’s raw attention maps contain rich structural cues, they also include substantial structural noise irrelevant to the target semantics. Without the semantic guidance provided by CAF and BCDR, directly merging DINO with CLIP can interfere with accurate semantic discrimination. This performance degradation further highlights the necessity of CAF and BCDR for early and deep cross-model interaction.

**Analysis of Structural Branch Selection.** Within our full framework, comparing different DINO variants reveals the importance of spatial consistency. As shown in Table 1, both SDCI-v1 and SDCI-v2 obtain higher accuracy than existing methods, the SDCI-v2 which is equipped with DINO-v2 gets slightly higher accuracy than SDCI-v1. Via the analysis on the detailed architectures of DINO and CLIP, we give the following two reasons. First, it is crucial to strike the best trade-off between semantic discriminability and spatial granularity: while DINO-v1 ( $8 \times 8$ ) preserves abundant fine-grained texture details, DINO-v2 ( $14 \times 14$ ) benefits from stronger pretrained representations and excels at object-level visual modeling. The notable gain in feature discriminability outweighs the marginal impact caused by reduced spatial resolution. Second, since the baseline CLIP model also adopts a  $14 \times 14$  patch size, DINO-v2 naturally aligns with CLIP feature maps on the spatial grid. This point-to-point correspondence completely avoids the up/down-sampling operations required by DINO-v1 during cross-modal fusion, thereby eliminating spatial misalignment and noise introduced by interpolation artifacts.

**Improved Semantic Generalization.** As shown in Table 2, under the generalized-label setting, our full method (66.40%) achieves a more substantial improvement over the baseline (56.82%), yielding a gain of +9.58%. Moreover, as shown in Table 1, our SDCI-v1 obtains the highest accuracy than existing methods on all the datasets except for Potsdam, and our SDCI-v2 obtains higher accuracy than existing

methods on all the datasets in the original-label setting. This demonstrates the strong robustness of our framework with respect to different quality of text prompts. In particular, CSCP helps preserve stable segmentation boundaries by leveraging intrinsic geometric cues, even when text prompts vary and lead to fluctuations in CLIP’s initial confidence. In this way, our method effectively mitigates the negative impact brought by the semantic gap.

**Gen vs. Candidate Set of Gen.** By comparing the performance under the generalized-label (Gen) setting and the “Set of Gen” settings, we observe a consistent trend: using our carefully selected best prompts (Gen) generally outperforms using the entire candidate set. For example, our final model (SDCI-v2) achieves an mIoU of 66.40% under the Gen setting, higher than 64.10% under the “Set of Gen” setting. This finding provides an important insight that *the quality of text prompts matters more than their quantity*. Feeding a candidate set with imprecise prompts as input can instead introduce semantic noise, dilute the core visual concept, and consequently interfere with the model predictions. Notably, when using the “Set of Gen” setting, the text embedding of each text prompt in the set are derived. Then, all the embeddings are averaged to produce the finally text embedding of each category.

## 5. Conclusion

This paper introduces a novel training-free multi-stage collaborative inference framework, termed SDCI, which aims to deeply fuse the semantic knowledge of CLIP with the structural knowledge of DINO, while further exploiting low-level geometric cues to tackle the challenge of OVSS in remote sensing imagery. Extensive experiments on multiple challenging benchmarks demonstrate that SDCI consistently outperforms existing methods under a training-free setting. Ablation studies further validate the positive effects of each module in SDCI and provide detailed analyses on the choice of the structural branch, and the improvement in semantic generalization. Despite the superior accuracy achieved by SDCI, it is undeniable that current training-free OVSS methods still lag behind traditional fully supervised approaches trained on specific datasets. Future work will focus on narrowing this performance gap.

## References

Abbasi, R., Nazari, A., Sefid, A., Banayeeanzade, M., Rohban, M. H., and Baghshah, M. S. CLIP Under the Microscope: A Fine-Grained Analysis of Multi-Object Representation. In *Proceedings of the IEEE/CVF Conference on Computer Vision and Pattern Recognition (CVPR)*, pp. 9308–9317, June 2025.

Barsellotti, L., Amoroso, R., Baraldi, L., and Cucchiara, R. FOSSIL: Free Open-Vocabulary Semantic Segmentation through Synthetic References Retrieval. In *IEEE/CVF Winter Conference on Applications of Computer Vision, WACV 2024, Waikoloa, HI, USA, January 3-8, 2024*, pp. 1453–1462. IEEE, 2024a. doi: 10.1109/WACV57701.2024.00149. URL <https://doi.org/10.1109/WACV57701.2024.00149>.

Barsellotti, L., Amoroso, R., Cornia, M., Baraldi, L., and Cucchiara, R. Training-Free Open-Vocabulary Segmentation with Offline Diffusion-Augmented Prototype Generation. In *Proceedings of the IEEE/CVF Conference on Computer Vision and Pattern Recognition (CVPR)*, pp. 3689–3698, June 2024b.

Barsellotti, L., Bianchi, L., Messina, N., Carrara, F., Cornia, M., Baraldi, L., Falchi, F., and Cucchiara, R. Talking to DINO: Bridging Self-Supervised Vision Backbones with Language for Open-Vocabulary Segmentation. In *Proceedings of the IEEE/CVF International Conference on Computer Vision (ICCV)*, pp. 22025–22035, October 2025.

Caron, M., Touvron, H., Misra, I., Jegou, H., Mairal, J., Bojanowski, P., and Joulin, A. Emerging properties in self-supervised vision transformers. In *2021 IEEE/CVF International Conference on Computer Vision (ICCV)*, pp. 9630–9640, 2021. doi: 10.1109/ICCV48922.2021.00951.

Chambolle, A. and Pock, T. A first-order primal-dual algorithm for convex problems with applications to imaging. *Journal of Mathematical Imaging and Vision*, 40(1):120–145, 2011. doi: 10.1007/s10851-010-0251-1. URL <https://doi.org/10.1007/s10851-010-0251-1>.

Felzenszwalb, P. F. and Huttenlocher, D. P. Efficient Graph-Based Image Segmentation. *International Journal of Computer Vision*, 59(2):167–181, September 2004. ISSN 1573-1405. doi: 10.1023/B:VISI.0000022288.19776.77. URL <https://doi.org/10.1023/B:VISI.0000022288.19776.77>.

Fu, S., Hamilton, M., Brandt, L. E., Feldmann, A., Zhang, Z., and Freeman, W. T. FeatUp: A Model-Agnostic Framework for Features at Any Resolution. In *The Twelfth International Conference on Learning Representations*, 2024. URL <https://openreview.net/forum?id=GkJiNn2QDF>.

Ge, J., Xie, L., Xie, H., Li, P., Liu, S.-A., Zhang, X., Tian, Q., and Zhang, Y. CLIP-Adapted Region-to-Text Learning for Generative Open-Vocabulary Semantic Segmentation. In *Proceedings of the IEEE/CVF International Conference on Computer Vision (ICCV)*, pp. 24034–24044, October 2025.

Hajimiri, S., Ayed, I. B., and Dolz, J. Pay Attention to Your Neighbours: Training-Free Open-Vocabulary Semantic Segmentation. In *2025 IEEE/CVF Winter Conference on Applications of Computer Vision (WACV)*, pp. 5061–5071, 2025. URL <https://api.semanticscholar.org/CorpusID:269137404>.

Kang, D. and Cho, M. In Defense of Lazy Visual Grounding for Open-Vocabulary Semantic Segmentation. In *Computer Vision – ECCV 2024: 18th European Conference, Milan, Italy, September 29–October 4, 2024, Proceedings, Part XLI*, pp. 143–164, Berlin, Heidelberg, 2024. Springer-Verlag. ISBN 978-3-031-72939-3. doi: 10.1007/978-3-031-72940-9\_9. URL [https://doi.org/10.1007/978-3-031-72940-9\\_9](https://doi.org/10.1007/978-3-031-72940-9_9).

Karazija, L., Laina, I., Vedaldi, A., and Rupprecht, C. Diffusion Models for Open-Vocabulary Segmentation. In Leonardis, A., Ricci, E., Roth, S., Russakovsky, O., Sattler, T., and Varol, G. (eds.), *Computer Vision – ECCV 2024*, pp. 299–317, Cham, 2025. Springer Nature Switzerland. ISBN 978-3-031-72652-1.

Kim, C., Ju, D., Han, W., Yang, M.-H., and Hwang, S. J. Distilling Spectral Graph for Object-Context Aware Open-Vocabulary Semantic Segmentation. In *IEEE/CVF Conference on Computer Vision and Pattern Recognition, CVPR 2025, Nashville, TN, USA, June 11–15, 2025*, pp. 15033–15042. Computer Vision Foundation / IEEE, 2025. doi: 10.1109/CVPR52734.2025.01400. URL [https://openaccess.thecvf.com/content/CVPR2025/html/Kim\\_Distilling\\_Spectral\\_Graph\\_for\\_Object-Context\\_Aware\\_Open-Vocabulary\\_Semantic\\_Segmentation\\_CVPR\\_2025\\_paper.html](https://openaccess.thecvf.com/content/CVPR2025/html/Kim_Distilling_Spectral_Graph_for_Object-Context_Aware_Open-Vocabulary_Semantic_Segmentation_CVPR_2025_paper.html).

Kirillov, A., Mintun, E., Ravi, N., Mao, H., Rolland, C., Gustafson, L., Xiao, T., Whitehead, S., Berg, A. C., Lo, W.-Y., Dollár, P., and Girshick, R. B. Segment Anything. In *2023 IEEE/CVF International Conference on Computer Vision (ICCV)*, pp. 3992–4003, 2023. URL <https://api.semanticscholar.org/CorpusID:257952310>.

Lan, M., Chen, C., Ke, Y., Wang, X., Feng, L., and Zhang, W. Proxyclip: Proxy attention improves clip for open-vocabulary segmentation. In *European Conference on Computer Vision*, pp. 70–88. Springer, 2024.

Lan, M., Chen, C., Ke, Y., Wang, X., Feng, L., and Zhang, W. ClearCLIP: Decomposing CLIP Representations for Dense Vision-Language Inference. In Leonardis, A., Ricci, E., Roth, S., Russakovsky, O., Sattler, T., and

Varol, G. (eds.), *Computer Vision – ECCV 2024*, pp. 143–160, Cham, 2025. Springer Nature Switzerland. ISBN 978-3-031-72970-6.

Li, K., Liu, R., Cao, X., Bai, X., Zhou, F., Meng, D., and Wang, Z. SegEarth-OV: Towards Training-Free Open-Vocabulary Segmentation for Remote Sensing Images. In *Proceedings of the Computer Vision and Pattern Recognition Conference (CVPR)*, pp. 10545–10556, June 2025.

Oquab, M., Darct, T., Moutakanni, T., Vo, H. V., Szafraniec, M., Khalidov, V., Fernandez, P., HAZIZA, D., Massa, F., El-Nouby, A., Assran, M., Ballas, N., Galuba, W., Howes, R., Huang, P.-Y., Li, S.-W., Misra, I., Rabbat, M., Sharma, V., Synnaeve, G., Xu, H., Jegou, H., Mairal, J., Labatut, P., Joulin, A., and Bojanowski, P. DINOv2: Learning Robust Visual Features without Supervision. *Transactions on Machine Learning Research*, 2024. ISSN 2835-8856. URL <https://openreview.net/forum?id=a68SUT6zFt>.

Radford, A., Kim, J. W., Hallacy, C., Ramesh, A., Goh, G., Agarwal, S., Sastry, G., Askell, A., Mishkin, P., Clark, J., Krueger, G., and Sutskever, I. Learning transferable visual models from natural language supervision. In Meila, M. and Zhang, T. (eds.), *Proceedings of the 38th International Conference on Machine Learning*, volume 139 of *Proceedings of Machine Learning Research*, pp. 8748–8763. PMLR, 18–24 Jul 2021. URL <https://proceedings.mlr.press/v139/radford21a.html>.

Ravi, N., Gabeur, V., Hu, Y.-T., Hu, R., Ryali, C., Ma, T., Kedr, H., Rädle, R., Rolland, C., Gustafson, L., Mintun, E., Pan, J., Alwala, K. V., Carion, N., Wu, C.-Y., Girshick, R., Dollár, P., and Feichtenhofer, C. Sam 2: Segment anything in images and videos. *arXiv preprint arXiv:2408.00714*, 2024. URL <https://arxiv.org/abs/2408.00714>.

Rombach, R., Blattmann, A., Lorenz, D., Esser, P., and Ommer, B. High-Resolution Image Synthesis With Latent Diffusion Models. In *Proceedings of the IEEE/CVF Conference on Computer Vision and Pattern Recognition (CVPR)*, pp. 10684–10695, June 2022.

Rottensteiner, F., Sohn, G., Gerke, M., and Wegner, J. D. The ISPRS benchmark on urban object detection and 3D building reconstruction. *ISPRS Journal of Photogrammetry and Remote Sensing*, 93:143–171, 2014. doi: 10.1016/j.isprsjprs.2013.10.004.

Shao, T., Tian, Z., Zhao, H., and Su, J. Explore the Potential of CLIP for Training-Free Open Vocabulary Semantic Segmentation. In Leonardis, A., Ricci, E., Roth, S., Russakovsky, O., Sattler, T., and Varol, G. (eds.), *Computer Vision – ECCV 2024*, pp. 139–156, Cham, 2025. Springer Nature Switzerland. ISBN 978-3-031-73016-0.

Shi, J. and Malik, J. Normalized cuts and image segmentation. *IEEE Transactions on Pattern Analysis and Machine Intelligence*, 22(8):888–905, 2000. doi: 10.1109/34.868688.

Shi, Y., Dong, M., and Xu, C. Harnessing Vision Foundation Models for High-Performance, Training-Free Open Vocabulary Segmentation. In *Proceedings of the IEEE/CVF International Conference on Computer Vision (ICCV)*, pp. 23487–23497, October 2025.

Shin, G., Xie, W., and Albanie, S. ReCo: Retrieve and Co-segment for Zero-shot Transfer. In Koyejo, S., Mohamed, S., Agarwal, A., Belgrave, D., Cho, K., and Oh, A. (eds.), *Advances in Neural Information Processing Systems*, volume 35, pp. 33754–33767. Curran Associates, Inc., 2022. URL [https://proceedings.neurips.cc/paper\\_files/paper/2022/file/daabe43c3e1d06980aa23880bfbe1f45-Paper-Conference.pdf](https://proceedings.neurips.cc/paper_files/paper/2022/file/daabe43c3e1d06980aa23880bfbe1f45-Paper-Conference.pdf).

Siméoni, O., Puy, G., Vo, H. V., Roburin, S., Gidaris, S., Bursuc, A., Pérez, P., Marlet, R., and Ponce, J. Localizing Objects with Self-supervised Transformers and no Labels. In *32nd British Machine Vision Conference 2021, BMVC 2021, Online, November 22–25, 2021*, pp. 310. BMVA Press, 2021. URL <https://www.bmvc2021-virtualconference.com/assets/papers/1339.pdf>.

Siméoni, O., Sekkat, C., Puy, G., Vobecký, A., Zablocki, É., and P'erez, P. Unsupervised Object Localization: Observing the Background to Discover Objects. *2023 IEEE/CVF Conference on Computer Vision and Pattern Recognition (CVPR)*, pp. 3176–3186, 2022. URL <https://api.semanticscholar.org/CorpusID:254685799>.

Siméoni, O., Vo, H. V., Seitzer, M., Baldassarre, F., Oquab, M., Jose, C., Khalidov, V., Szafraniec, M., Yi, S., Ramamonjisoa, M., Massa, F., Haziza, D., Wehrstedt, L., Wang, J., Darct, T., Moutakanni, T., Sentana, L., Roberts, C., Vedaldi, A., Tolan, J., Brandt, J., Couprie, C., Mairal, J., Jegou, H., Labatut, P., and Bojanowski, P. DINOv3, 2025. URL <https://arxiv.org/abs/2508.10104>. eprint: 2508.10104.

Sun, L., Cao, J., Xie, J., Jiang, X., and Pang, Y. CLIPer: Hierarchically Improving Spatial Representation of CLIP for Open-Vocabulary Semantic Segmentation. In *Proceedings of the IEEE/CVF International Conference on Computer Vision (ICCV)*, pp. 23199–23209, October 2025.

Sun, S., Li, R., Torr, P., Gu, X., and Li, S. CLIP as RNN: Segment Countless Visual Concepts without Training Endeavor. *2024 IEEE/CVF Conference on Computer Vision and Pattern Recognition (CVPR)*, pp. 13171–13182, 2023. URL <https://api.semanticscholar.org/CorpusID:266191302>.

Tong, X.-Y., Xia, G.-S., Lu, Q., Shen, H., Li, S., You, S., and Zhang, L. Land-cover classification with high-resolution remote sensing images using transferable deep models. *Remote Sensing of Environment*, 237:111322, 2020. ISSN 0034-4257. doi: <https://doi.org/10.1016/j.rse.2019.111322>. URL <https://www.sciencedirect.com/science/article/pii/S0034425719303414>.

Wang, F., Mei, J., and Yuille, A. SCLIP: Rethinking Self-Attention for Dense Vision-Language Inference. In Leonardis, A., Ricci, E., Roth, S., Russakovsky, O., Sattler, T., and Varol, G. (eds.), *Computer Vision – ECCV 2024*, pp. 315–332, Cham, 2025. Springer Nature Switzerland. ISBN 978-3-031-72664-4.

Wang, J., Zheng, Z., Ma, A., Lu, X., and Zhong, Y. LoveDA: A Remote Sensing Land-Cover Dataset for Domain Adaptive Semantic Segmentation. In Vanschoren, J. and Yeung, S. (eds.), *Proceedings of the Neural Information Processing Systems Track on Datasets and Benchmarks*, volume 1. Curran Associates, Inc., 2021. URL [https://datasets-benchmarks-proceedings.neurips.cc/paper\\_files/paper/2021/file/4e732ced3463d06de0ca9a15b6153677-Paper-round2.pdf](https://datasets-benchmarks-proceedings.neurips.cc/paper_files/paper/2021/file/4e732ced3463d06de0ca9a15b6153677-Paper-round2.pdf).

Wang, X., Girdhar, R., Yu, S. X., and Misra, I. Cut and learn for unsupervised object detection and instance segmentation. In *Proceedings of the IEEE/CVF Conference on Computer Vision and Pattern Recognition*, pp. 3124–3134, 2023a.

Wang, X., Misra, I., Zeng, Z., Girdhar, R., and Darrell, T. VideoCutLER: Surprisingly Simple Unsupervised Video Instance Segmentation . In *2024 IEEE/CVF Conference on Computer Vision and Pattern Recognition (CVPR)*, pp. 22755–22764, Los Alamitos, CA, USA, June 2024. IEEE Computer Society. doi: 10.1109/CVPR52733.2024.02147. URL <https://doi.ieee.org/10.1109/CVPR52733.2024.02147>.

Wang, Y., Shen, X. I., Hu, S. X., Yuan, Y., Crowley, J. L., and Vaufreydaz, D. Self-Supervised Transformers for Unsupervised Object Discovery using Normalized Cut. *2022 IEEE/CVF Conference on Computer Vision and Pattern Recognition (CVPR)*, pp. 14523–14533, 2022. URL <https://api.semanticscholar.org/CorpusID:247058696>.

Wang, Y., Shen, X., Yuan, Y., Du, Y., Li, M., Hu, S. X., Crowley, J. L., and Vaufreydaz, D. TokenCut: Segmenting Objects in Images and Videos With Self-Supervised Transformer and Normalized Cut. *IEEE Transactions on Pattern Analysis and Machine Intelligence*, 45(12):15790–15801, December 2023b. ISSN 1939-3539. doi: 10.1109/TPAMI.2023.3305122.

Waqas Zamir, S., Arora, A., Gupta, A., Khan, S., Sun, G., Shahbaz Khan, F., Zhu, F., Shao, L., Xia, G.-S., and Bai, X. iSAID: A Large-scale Dataset for Instance Segmentation in Aerial Images. In *Proceedings of the IEEE Conference on Computer Vision and Pattern Recognition Workshops*, pp. 28–37, 2019.

Wysoczańska, M., Siméoni, O., Ramamonjisoa, M., Bursuc, A., Trzciński, T., and Pérez, P. CLIP-DINOiser: Teaching CLIP a Few DINO Tricks for Open-Vocabulary Semantic Segmentation. In Leonardis, A., Ricci, E., Roth, S., Russakovsky, O., Sattler, T., and Varol, G. (eds.), *Computer Vision – ECCV 2024*, pp. 320–337, Cham, 2025. Springer Nature Switzerland. ISBN 978-3-031-73030-6.

Xia, G.-S., Bai, X., Ding, J., Zhu, Z., Belongie, S., Luo, J., Datcu, M., Pelillo, M., and Zhang, L. DOTA: A Large-Scale Dataset for Object Detection in Aerial Images. In *The IEEE Conference on Computer Vision and Pattern Recognition (CVPR)*, 2018.

Yang, Y., Deng, J., Li, W., and Duan, L. ResCLIP: Residual Attention for Training-free Dense Vision-language Inference. *2025 IEEE/CVF Conference on Computer Vision and Pattern Recognition (CVPR)*, pp. 29968–29978, 2025. URL <https://api.semanticscholar.org/CorpusID:274234839>.

Zhang, D., Liu, F., and Tang, Q. CorrCLIP: Reconstructing Patch Correlations in CLIP for Open-Vocabulary Semantic Segmentation. In *Proceedings of the IEEE/CVF International Conference on Computer Vision (ICCV)*, pp. 24677–24687, October 2025a.

Zhang, W., Xiao, D., Chen, L., and Wang, L. E-sam: Training-free segment every entity model. In *Proceedings of the IEEE/CVF International Conference on Computer Vision (ICCV)*, pp. 24688–24697, October 2025b.

Zhong, D., Zheng, X., Liao, C., Lyu, Y., Chen, J., Wu, S., Zhang, L., and Hu, X. OmniSAM: Omnidirectional Segment Anything Model for UDA in Panoramic Semantic Segmentation. In *Proceedings of the IEEE/CVF International Conference on Computer Vision (ICCV)*, pp. 23892–23901, October 2025.

Zhou, C., Loy, C. C., and Dai, B. Extract Free Dense Labels from CLIP. In *Computer Vision – ECCV 2022: 17th European Conference, Tel Aviv, Israel, October 23–27, 2022, Proceedings, Part XXVIII*, pp. 696–712, Berlin, Heidelberg, 2022. Springer-Verlag. ISBN 978-3-031-19814-4. doi: 10.1007/978-3-031-19815-1\_40. URL [https://doi.org/10.1007/978-3-031-19815-1\\_40](https://doi.org/10.1007/978-3-031-19815-1_40).

## A. Detailed Description of the Modules in SDCI

Rather than treating CLIP and DINO as independent entities, CAF guides each model’s inference by injecting the other’s self-attention maps. Specifically, DINO’s fine-grained spatial attention is used to propagate CLIP’s semantic responses. Conversely, CLIP’s semantic attention injects an explicit category focus into DINO’s purely structural attention, aggregating originally scattered activations into coherent semantic regions. This process enables both branches to produce preliminary segmentation logic that already incorporates the advantages of the other.

BCDR conducts bidirectional and symmetric refinement via iterative random-walk diffusion: (i) we diffuse the semantic scores from the CLIP branch over a more reliable structural graph constructed by DINO to correct spatial inconsistencies; and (ii) we diffuse the structured scores from the DINO branch over a more strongly correlated semantic graph constructed by CLIP to merge semantically separated regions.

CSCP aims to address blurred boundaries and spatial inconsistency through global optimization. This module formulates segmentation refinement as a global convex optimization problem, whose energy function consists of two terms: (i) a KL-divergence data fidelity term based on the probabilistic predictions produced by BCDR, and (ii) an anisotropic total variation (Anisotropic TV) spatial regularization term constructed using superpixels. The former ensures that the refined results remain semantically faithful to the original high-quality predictions, while the latter enables adaptive edge preservation by enforcing smoothness within each superpixel while allowing sharp gradient changes along boundaries. Finally, the energy function is iteratively solved using the Primal–Dual Hybrid Gradient (PDHG) algorithm (Chambolle & Pock, 2011).

## B. Visualization of CAF’s Effect

As shown in Fig. 3(a), when CAF injects CLIP semantic information into DINO, the originally scattered similarity-based points are semantically aggregated, clearly delineating object boundaries. As shown in Fig. 3(b), when CAF injects DINO’s structural information into CLIP, objects similar to the current semantic category are also enhanced, enabling the promotion and generalization of CLIP semantic cues. This bidirectional (forward + backward) strategy not only achieves complementary information exchange, but also mitigates noise interference to some extent compared to the one-way process.

## C. Experimental Settings

### C.1. Datasets

To comprehensively evaluate the performance of SDCI across different sensors, spatial resolutions, and top-view scenarios, we conduct experiments on five widely used yet highly challenging remote sensing semantic segmentation datasets.

**GID** (Tong et al., 2020) is a large-scale high-resolution remote sensing dataset composed of wide-swath Gaofen-2 (GF-2) satellite imagery. Each large image has a size of  $6800 \times 7200$  pixels with a spatial resolution of 4 m. GID covers extensive geographic regions, and its main challenge lies in the pronounced intra-class heterogeneity, such as buildings with diverse architectural styles and farmlands at different growth stages. Therefore, we use this dataset to evaluate the model’s macroscopic recognition robustness in large-scale complex scenes.

**Potsdam** (Rottensteiner et al., 2014) is a classic high-resolution aerial image benchmark released by the International Society for Photogrammetry and Remote Sensing (ISPRS). With a spatial resolution of 0.5 m, it is widely used to evaluate the performance of fine-grained segmentation in urban scenes. Potsdam contains densely distributed buildings, roads, vehicles, and low vegetation, imposing stringent requirements on boundary localization accuracy and small-object recognition. It provides two modalities of remote sensing imagery, including true-color orthophotos with red–green–blue (R–G–B) channels and false-color orthophotos with near-infrared–red–green (IR–R–G) channels.

**Vaihingen** (Rottensteiner et al., 2014) is another highly challenging high-resolution aerial remote sensing benchmark provided by ISPRS. The Vaihingen dataset consists of false-color orthophotos with near-infrared–red–green (IR–R–G) channels, with a spatial resolution of 0.9 m. It mainly depicts well-spaced detached houses and small multi-storey residential areas with noticeable terrain undulations. Due to its unique spectral composition, this dataset emphasizes the model’s capability to extract features from non-visible bands and its robustness under complex shadows and irregularly distributed objects.

**LoveDA** (Wang et al., 2021) is a high-resolution satellite imagery dataset with a spatial resolution of 0.3 m. It is specifically designed for domain adaptation research and provides two distinct scenarios—urban and rural—from different geographic

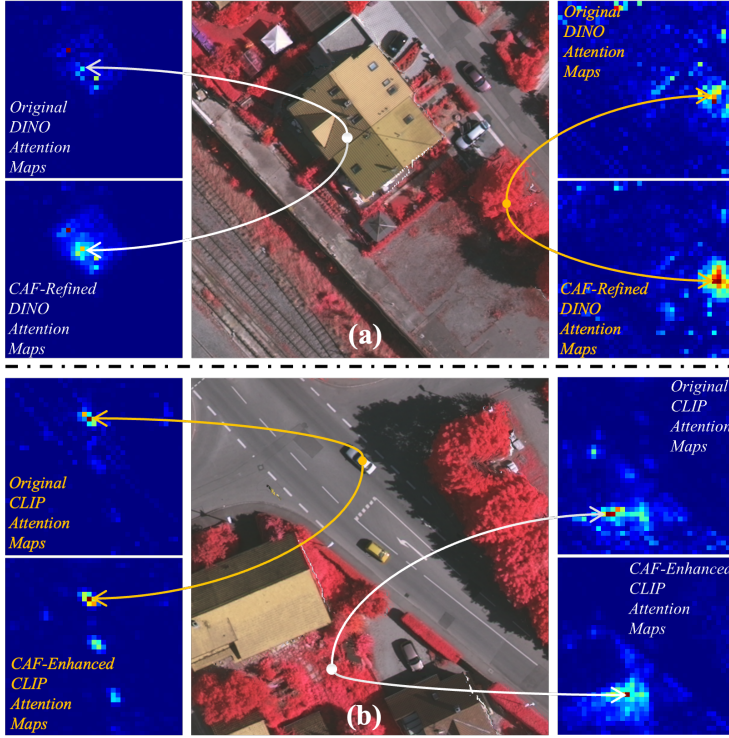


Figure 3. Visualization observations of CAF bidirectional cross-fusion. In (a), by introducing CLIP semantic priors, DINO’s originally scattered similarity-based structures are semantically aggregated, endowing the unsupervised features with explicit category guidance; in (b), after injecting DINO structural information, targets similar to the current semantic category are enhanced, enabling the spatial propagation of CLIP semantic cues.

regions. This design makes it an ideal benchmark for testing a model’s generalization ability under severe scene distribution shifts. We use this dataset to evaluate the cross-scene robustness of our method.

**iSAID** (Waqas Zamir et al., 2019) is a large-scale aerial image segmentation benchmark. Its images are collected from multiple aerial and satellite platforms based on the large-scale DOTA dataset (Xia et al., 2018), and thus it does not have a unified spatial resolution, ranging approximately from 0.1 m to 4 m. It is also one of the most challenging datasets in this field. iSAID contains 15 categories covering typical man-made objects such as airplanes, ships, storage tanks, bridges, and vehicles. iSAID is well known for its extreme scale variation and high-density object distribution, where massive infrastructure and tiny moving targets often co-exist in the same image. Such dramatic scale discrepancies and dense spatial layouts particularly stress the model’s capability of multi-scale feature aggregation and the upper-limit performance of pixel-level segmentation in crowded scenes.

## C.2. Metrics

We adopt a standard and widely used pixel-level evaluation metric, namely Mean Intersection over Union (mIoU) to quantitatively evaluate the segmentation performance. This metric first computes the Intersection over Union (IoU) for each class, defined as the ratio between the intersection and the union of the predicted region and the ground-truth region, and then averages the IoU values over all classes.

For a task with  $N_C$  classes, mIoU is calculated as:

$$\text{mIoU} = \frac{1}{N_C} \sum_{i=1}^{N_C} \frac{\text{TP}_i}{\text{TP}_i + \text{FP}_i + \text{FN}_i}, \quad (19)$$

where  $\text{TP}_i$ ,  $\text{FP}_i$ , and  $\text{FN}_i$  denote the numbers of true positive, false positive, and false negative pixels for class  $i$ , respectively.

### C.3. Implementation Details

SDCI is implemented based on PyTorch. All experiments are conducted on a computer equipped with four NVIDIA GeForce RTX 3090 GPU devices. To ensure fair comparisons and to validate the generalization ability of our method, all experiments follow a fixed set of hyperparameters as described below.

The dual-branch architecture of SDCI consists of a semantic branch and a structural branch. For the semantic branch, we adopt the CLIP ViT-L/14 model released by OpenAI as the backbone. For the structural branch, we evaluate two pretrained DINO models, including DINO-v1 and DINO-v2. It is worth noting that, to ensure that the output feature dimensions can be efficiently aligned with other components in our framework and to evaluate the performance evolution across DINO generations on a fair benchmark, we consistently use a ViT-Base backbone for the structural branch. In all experiments, the parameters of these backbone networks are frozen.

In SDCI, CAF is implemented via direct additive injection (i.e.,  $\lambda_1 = 1$  in Eqs. 8 and 9). For Eqs. 11-12 in BCDR, the default settings are  $K = 30$  and  $\tau = 7$ . For the diffusion process (i.e., Eqs. 13 and 14), the total number  $T$  of diffusion steps is set to 40, and the smoothing factor  $\alpha$  is set to 0.9. For Eqs. 16-18 in CSCP, the balancing coefficients  $\lambda_C$  and  $\lambda_D$  are set to 1.0 and 0.2, the total variation regularization strength  $\beta$  is set to 0.10, and the adaptive edge-weight parameters  $w_{\text{in}}$  and  $w_{\text{cross}}$  are set to 1.0 and 0.10, respectively. All input images are uniformly cropped to  $512 \times 512$  pixels. We adopt full-image inference, where the entire image is directly fed into the encoder.

### C.4. Design Process of Prompt Settings

To produce the prompt settings in Sec. 4.1, we design a two-stage prompt selection pipeline, as shown in Table 3. First, for each original name, we construct a generalized label candidate set (Set of Gen). This Set of Gen is centered around the core visual concept and includes potential prompts spanning multiple semantic dimensions (e.g., constituent elements, functionality, and hierarchical relations). Subsequently, the final generalized label (Gen) is determined from Set of Gen. For example, the *built-up* category in the GID dataset is visually almost entirely represented by well-defined individual buildings, and thus we choose *buildings* to achieve the most direct and unambiguous visual correspondence. In contrast, the *impervious surfaces* category in the Potsdam dataset constitutes a *heterogeneous composite* composed of roads, parking lots, and plazas. Therefore, we select a semantically richer prompt set  $\{\text{ground}, \text{road}, \text{streets}\}$  to holistically capture its diverse visual semantics. By comparison, for the iSAID dataset, since its category names (e.g., *plane*, *ship*) essentially correspond to concrete individual objects and are naturally aligned with the CLIP vocabulary space, we directly retain the official category names to avoid unnecessary semantic re-construction.

## D. Visual Comparisons with Existing Methods

Moreover, Fig. 4 presents visual comparisons of the segmentation results produced by our method and existing approaches. Given the large number of datasets and visualizations, we only showcase datasets on which one version of our method performs slightly worse than the best existing method as shown in Table 1. From the visual results, we still observe that SDCI produces more accurate boundaries and more reliable semantic predictions.

## E. Visual Results for Ablation Study

Fig. 5 visualizes the contributions of our individual modules. The baseline model (as shown in Fig. 5b) produces relatively coarse segmentation results with blurry boundaries and a large range of noises. As CAF, BCDR, and CSCP are progressively integrated, noise in the segmentation results is continuously suppressed, and the boundaries become increasingly clear. As a result, the full method achieves high visual agreement with the ground truth.

Table 3. Mapping details from the original (Ori) labels to the generalized (Gen) labels across different datasets. The Gen labels are manually designed to be more descriptive by decomposing complex or technical terms into concrete visual components, and are better aligned with the natural-language understanding of vision–language models, thereby forming a more realistic evaluation benchmark.

Dataset	Ori	Candidate Set of Gen	Gen
GID	built-up	residential area, structures, buildings, architecture	buildings
	farmland	cropland, agricultural land, field, cultivated land	agricultural land
	forest	woodland, tree cover, mountain forest, canopy	mountain forest
	meadow	grassland, greenspace, shrubs, flatland forest, low vegetation	flatland forest
	water	river, lake, water body	water body
Potsdam	impervious surfaces	road, streets, ground, parking lot, sidewalk	ground, road, streets
	building	buildings, man-made buildings, architecture, house	buildings, man-made buildings
	low vegetation	low vegetation, low-growing grassland, grass patches, lawn, grass vegetation	low vegetation, low-growing grassland, grass patches, lawn, grass vegetation
	tree	woods, trees, plants	trees
	car	automobile, vehicles, transportation	vehicles
Vaihingen	impervious surfaces	road, streets, ground, parking lot, sidewalk	ground, road, streets
	building	building, man-made buildings, architecture, house	building
	low vegetation	low vegetation, low-growing grassland, grass	low vegetation, low-growing grassland
	tree	woods, tree, plants	tree
	car	automobile, vehicles, transportation	vehicle
LoveDA	building	building, man-made buildings, architecture, house	building
	road	road, streets	road
	water	river, lake, water	water
	barren	bare land, dry soil, sandy land	dry soil
	forest	woodland, tree cover, forest	forest
	agriculture	cropland, agricultural land, field, farmland	farmland

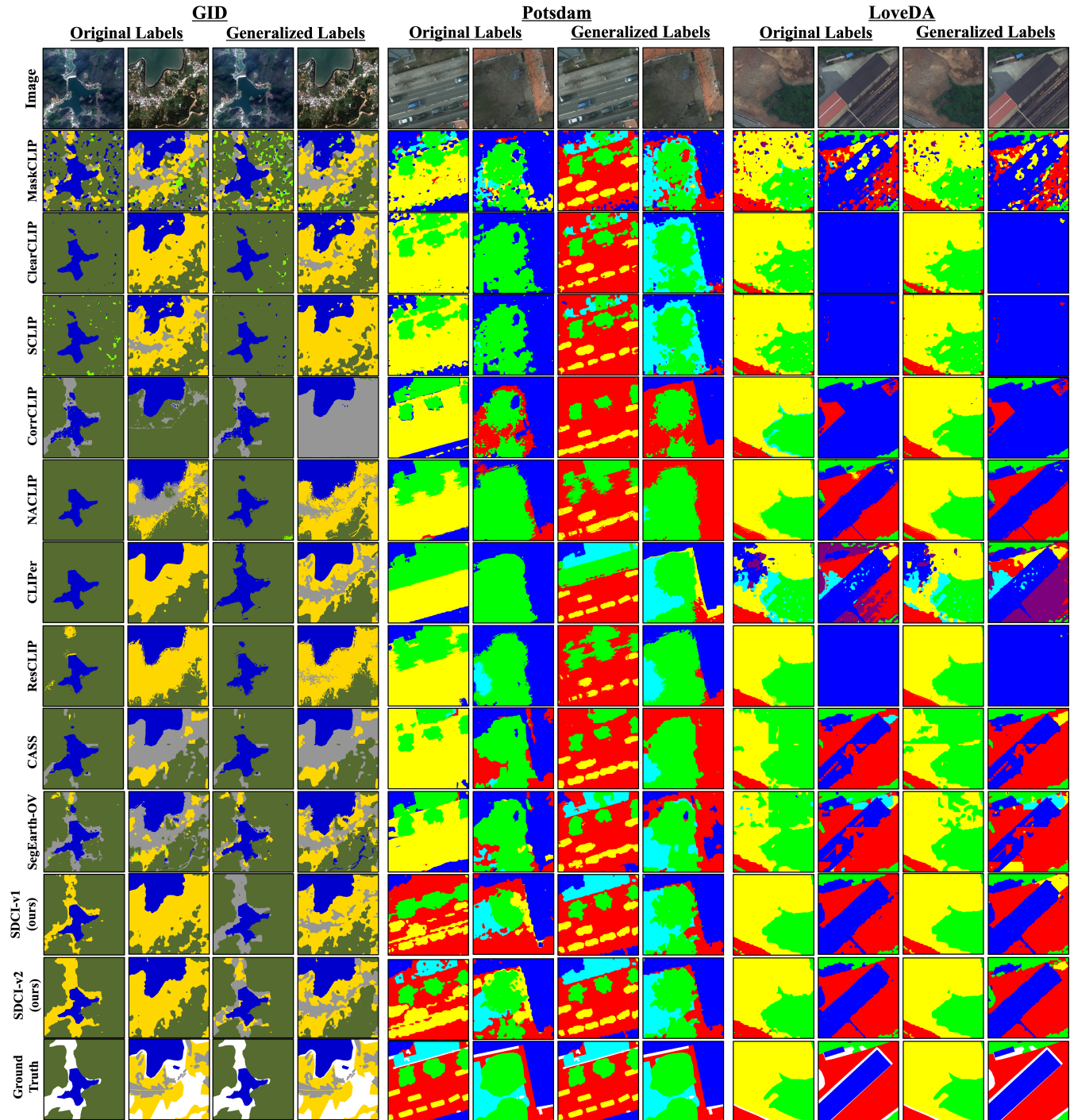


Figure 4. Visual comparison with existing methods.

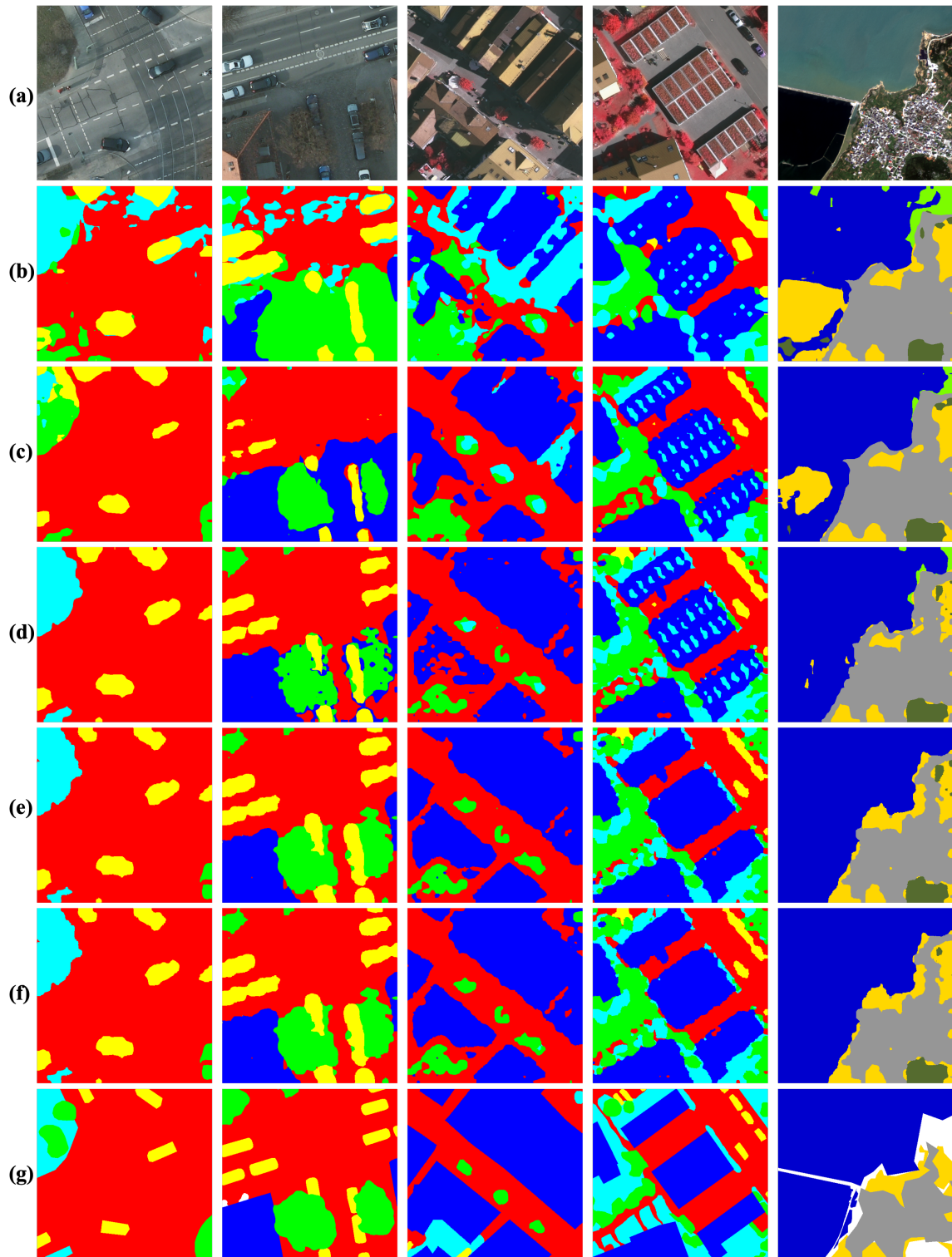


Figure 5. The visualization results of the ablation study. This visualization shows that, as the proposed modules are progressively added, the segmentation performance is continuously improved. (a) original image, (b) results of the baseline model, (c) results of baseline + CAF, (d) results of baseline + CAF + BCDR, (e) full model with CSCP (SDCI-v1), (f) full model with CSCP (SDCI-v2), (g) ground truth.